# NUMERICAL AND EXPERIMENTAL INVESTIGATIONS OF TWIN-ENGINE-LIGHT UTILITY HELICOPTER WAKE FLOW

M. Stuhlpfarrer, A. Kümmel, J. Steck, C. Breitsamter
Institute of Aerodynamics and Fluid Mechanics, Technische Universität München

**Abstract**

The present paper concentrates on the unsteady characteristics of the wake flow field emanating from a helicopter fuselage and rotor head. Predicting the convection of blade tip vortices and other coherent structures generated by the fuselage and the rotor head is difficult by applying numerical methods. Therefore, numerical and experimental investigations have been carried out on a twin-engine-light utility helicopter to provide a data base for code validation. The wind tunnel model includes a fuselage and a rotating five-bladed rotor head. The latter allows cyclic and collective pitch motion. The numerical investigations are performed with ANSYS Fluent. The flow solver is based on the unsteady Reynolds-averaged Navier-Stokes equations. Turbulence modelling is performed with the shear stress transport model and the scale adaptive simulation model.

**Nomenclature**

| | |
|---|---|
| $C_\mu$ | Specified constant for shear stress transport model ($C_\mu = 0.09$) |
| $d$ | Diameter |
| $k$ | Turbulence kinetic energy |
| $l$ | Length |
| $Ma$ | Mach number |
| $Re$ | Reynolds number |
| $U_\infty$ | Free stream velocity |
| $u, v, w$ | Cartesian velocity components |
| $x, y, z$ | Cartesian coordinates |
| $\lambda$ | Advancing ratio |
| $\mu_t/\mu$ | Eddy viscosity ratio |
| $\omega$ | Turbulence eddy frequency |

## 1. INTRODUCTION

The knowledge of the wake flow of helicopters is important concerning the unsteady effects. Due to the interaction of the wake flow with the helicopter itself, comfort and safety issues require accurate information already in the design process [1]. Previous experimental and numerical investigations have been performed on twin-engine-light utility helicopter configurations which showed well results for steady and unsteady flow quantities [2], [3], [4].

Nevertheless, the precise prediction of the wake flow is a difficult goal by applying computational fluid dynamics. Especially, due to the variety of different flow regimes, i.e. laminar or turbulent and attached or separated flow, separation the best suited modelling approach has to be found.

An important unsteady phenomenon is tail shake. It occurs if coherent structures emanating of the rotor or the fuselage impinge at the stabilizer of the helicopter. In order to capture this effect, the numerical simulation has to predict the origin of that flow phenomenon in the right way as well as the downstream convection of these coherent structures. These goals are difficult to fulfil. Firstly, for flows with laminar-turbulent transition and separation the state of the art turbulence models cannot resolve these effects appropriately. Secondly, the numerical dissipation of the applied discretization scheme may affect the loss of information during the convection of the flow [5]. In order to overcome these difficulties low dissipative numerical schemes and scale resolving turbulence models shall be applied.

In the present work the focus is set on characterizing and analyzing the flow of the near wake field of a novel twin-engine light utility helicopter configuration. Therefore, experimental and numerical investigations are performed. The experimental data obtained from particle image velocimetry (PIV) measurements are used to characterize the near wake flow downstream of the helicopter. These results are complemented with numerical results gained by solving the unsteady Reynolds-averaged Navier-Stokes (URANS) equations.

## 2. EXPERIMENTS

In this section the helicopter configuration and the test facility are described. Furthermore, the particle image velocimetry system and test conditions are provided.

### 2.1. Helicopter Configuration and Facility

The experiments are performed on a 1:5 scale detailed model of a characteristic twin-engine-light (TEL) utility helicopter. Major parts of the baseline model include front and main cabin section, back door section, upper cowling, mast fairing, 5-bladed rotor head and skid landing gear. The model fuselage parts are made of composite material connected to an inner load bearing frame made of aluminum. A tail sting element located inside the tail boom is used to attach the model frame to the model support. The rotor head allows for collective and cyclic pitch motion of blade cuffs using a fully functional swash blade. The blade cuffs are truncated at the radial position of the first effective aerodynamic blade section. Furthermore, this model includes an aerodynamic optimized shape at the back door section with contoured strakes [6].

Figure 1 shows the wind tunnel configuration in the wind tunnel test section. It is sting mounted on a six component underfloor balance. It is further used for setting the angle of attack and angle of sideslip in combination with a second actuator in the sting.

**Figure 1: Helicopter model mounted in the wind tunnel test section**

The wind tunnel investigations have been carried out in the large low speed facility A of the Institute of Aerodynamics and Fluid Mechanics (AER) of the Technische Universität München (TUM). Test section dimensions are 1.8 m in height, 2.4 m in width and 4.8 m in length. Here, this closed return wind tunnel (Göttingen type) is operated with an open test section. The turbulence level is less than 0.4%. The uncertainty in the spatial and temporal mean velocity distribution is less than 0.067%.

Figure 2 presents the plan view of the wind tunnel including the measures.

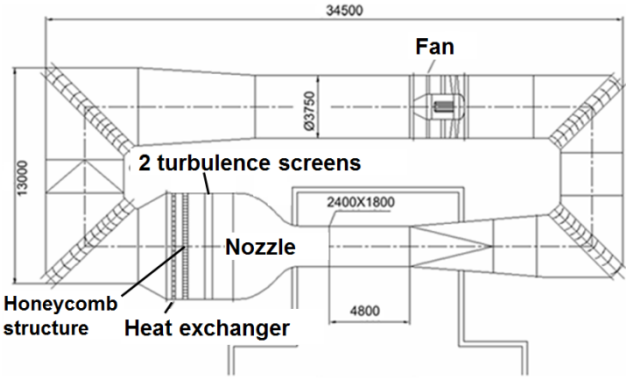


**Figure 2: Plan view of the Wind Tunnel A**

### 2.2. Stereo Particle Image Velocimetry and Test Conditions

In order to determine the velocities in the wake flow, Stereo-PIV is used. The PIV system contains a 325 mJ double cavity Nd:YAG laser with a wavelength of 532 nm and a maximum double pulse frequency of 15 Hz. Furthermore, it contains an adjustable laser beam guiding arm with light sheet optics mounted on a three axis traverse system. For these investigations, the laser was operated with an averaged double pulse frequency of approximately 4 Hz. The light sheet thickness is set to approximately 3 mm and the pulse delay is set to 10 μs. A synchronization unit is used for laser and camera synchronization and internal triggering. Images are recorded with an average frequency of approximately 4 Hz. The images are obtained from two sCMOS cameras with a resolution of 2560 x 2160 pixels resulting in a spatial resolution of 3.5 mm. The velocity fields are averaged for 400 data samples.

The inflow velocity and the rotational speed of the rotor are set to fulfil an advancing ratio of 0.35 at ambient pressure and temperature. The freestream Reynolds number is $Re \approx 1 \cdot 10^6$ based on the characteristic length derived from the cross section of the model.

## 3. NUMERICAL METHODS

This section gives a brief description of the numerical model. Nextly, a detailed explanation of the meshing methodology is given. Lastly, the solver settings are described.

The numerical simulations are performed with the commercial software ANSYS Fluent. The numerical grids are generated with ANSYS ICEM CFD. For this purpose, a block-structured hexahedron mesh is applied. The grid is divided into three parts which are connected by sliding mesh interfaces. The static domain contains the helicopter configuration. Furthermore, a rotating disk is embedded to model the motion of the rotor. Therein, an additional domain is designed which realizes the cyclic movement of each rotor blade. Figure 3 shows the helicopter configuration used for the numerical simulations. The geometry of the model contains the fuselage, the landing skid and the rotor head. In comparison to the experimental setup some simplifications for the rotor head are made. Figure 4 shows the simplified rotor head geometry with the truncated blades. It presents the hub cap, dampers, steering rods, scissors and rotor shaft with swash blade.

**Figure 3: Helicopter geometry used for the numerical simulations**

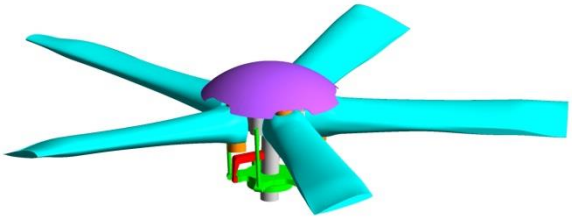

**Figure 4: Simplified rotor head geometry for the numerical simulations**

### 3.1. Meshing Methodology

In the following a detailed description of the blocking and meshing approach is given. As mentioned before, the mesh will consist of different parts which move with relative velocities to each other. Each mesh is generated with ICEM CFD and consists of hexahedron elements only. Figure 5 shows the static domain representing the far field around the helicopter. The dimensions of the domains are chosen in accordance to the size of the wind tunnel test section.

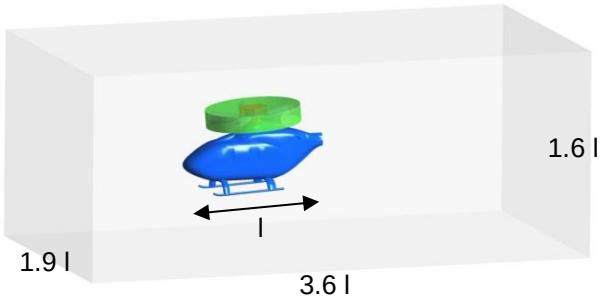


**Figure 5: Stationary Domain (grey) and with embedded disc domain (green)**

The rotor head including the truncated blade cuffs is embedded in the green high-lighted domain. In order to overcome the complexity of the geometry during the grid generation the rotor head is divided into several mesh parts that are merged together by a non-conformal interface. For the upper part of the rotor head and the hub cap as well as for the disk domain the periodicity was used for meshing. For the lower part of the rotor head it has to be meshed without using periodicity due to the scissors.

Figure 6 exhibits the blocking of the upper rotor head and the hub cap domain (URHD). Furthermore, a simplified connection of the blade and the mast, the dampers and the upper part of the steering rods are included.

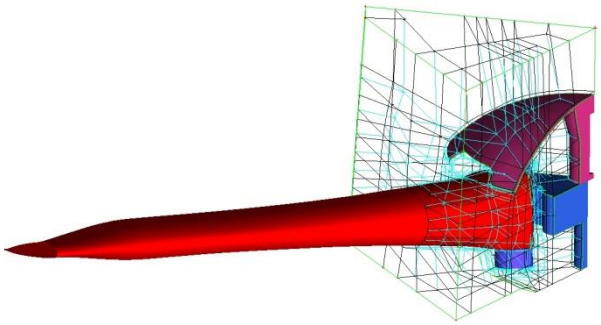

**Figure 6: Blocking of the upper rotor head domain.**

Figure 7 shows the blocking of the domain around the truncated blade (BD). This domain is embedded in the rotating disk domain. Figure 8 depicts the disk domain including the blade domain. The upper rotor head domain, the blade domain as well as the disk

domian (DD) are rotated four times to obtain the complete mesh.

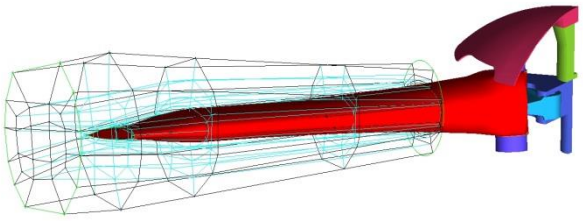

**Figure 7: Blocking of the blade domain that allows cyclic and collective pitch motion.**

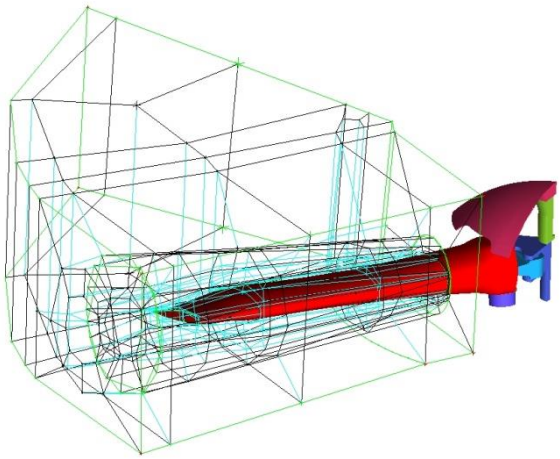

**Figure 8: Blocking of the rotating disk domain with the embedded blade domain.**

The blocking of the lower rotor head domain (LRHD) is presented in Figure 9. It includes the swashplate, the lower part of the steering rods and the scissors.

This approach allows modelling the cyclic and the collective pitch motion of the blade. The LRHD is connected to the URHD by a non-conformal interface. Between the BD and both DD a sliding mesh interface could be chosen in order to model the cyclic motion of the blade. For this case the interface type has to be applied between the BD and the URHD as well. The motion of the swash blade and scissors is realized by deforming mesh.

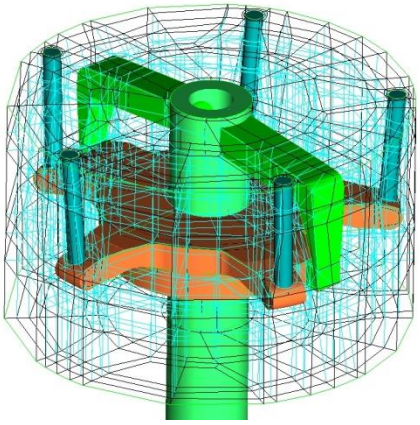

**Figure 9: Blocking of the lower rotor head domain including the swashblade, the mast and the scissors as well as lower parts of the steering rods.**

In the course of these investigations, the URHD and the LRHD are rigid domains. Further, the BD including the blades performs no cyclic motion. Nevertheless, the blocking is constructed for deforming mesh motion in the rotor head region.

The $y^+$-values in the domains are set to approximately one that a wall function has not to be used. Nevertheless, in certain regions it is greater than one. Furthermore, the ratio of the cell length at the interfaces is set to approximately one. This is especially important to reduce the numerical error at the interface in combination with less dissipative numerical schemes. Furthermore, the estimated turbulence length scale in the wake region is taken into account for estimating the cell sizes.

### 3.2. Equation Solving

The numerical investigations are performed by solving the URANS equations. For this purpose, the commercial flow solver ANSYS Fluent is used. The flow is assumed to be incompressible since the $Ma < 0.3$ in the whole domain. The pressure-velocity coupling is treated by applying the SIMPLE algorithm. In order to reduce numerical dissipation for the spatial discretization a second order upwind scheme is chosen. For the temporal discretization a bounded second order implicit scheme is used. It blends depending on the solution between first and second order to prevent spurious oscillations. For the turbulence modelling, the k-$\omega$ shear stress transport (SST) model is applied. The occurring transport equations for the turbulence kinetic energy as well as the turbulence eddy frequency are discretized by a first order upwind scheme. Additionally, simulations with the scale adaptive simulation (SAS) model are executed. In order to reduce the numerical dissipation error further, a

bounded central difference scheme is chosen to discretize the momentum equations. The flow is assumed to be fully turbulent. The time step is chosen such that the incompressible Courant number is $Co < 1$ in the wake flow field [7], [8], [9].

The boundary conditions are set according to the experimental setup. At the inlet the velocity is prescribed in order to fulfil the advancing ratio in combination with the rotational speed of the rotor head. At the outlet a pressure outlet boundary condition is applied. On the remaining boundaries of the box a free slip wall boundary condition is used.

## 4. RESULTS AND DISCUSSION

In the following chapter, the results of the experimental as well as of the numerical simulations are described and compared. Especially, the wake flow of the skid landing gear and the back door section is presented in detail. Additionally, the wake flow field of the rotor head is described briefly.

### 4.1. Results of the Wind Tunnel Tests

In the course of this investigation three streamwise positioned crossflow planes behind the back cabin door section and one in the wake of the rotor head are measured. The locations are shown schematically in Figure 10.

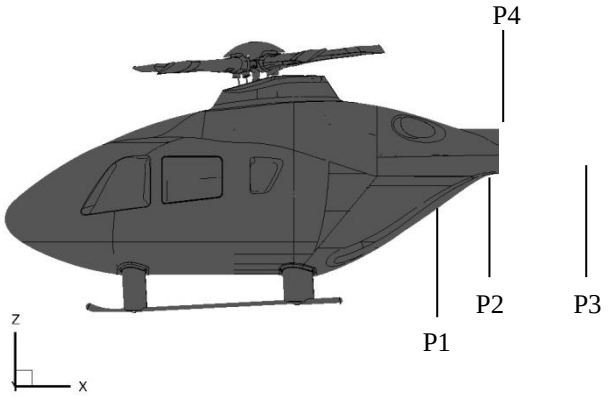


**Figure 10: Definition of the PIV planes.**

Figure 11 presents the normalized axial velocity. The wake flow of the back door section produces a small region of velocity deficit. This means that the flow stays attached in this region. There are two different structures appearing in the wake flow of the skid landing gear. The first structure is positioned downstream of the skid landing gear. The second structure becomes visible between the skids of the landing gear. The magnitude of the normalized axial velocity is less for this second mentioned structure. Due to the relatively small regions of the reduced axial velocity component the drag of the back door section is less compared to a configuration without strakes. The reason for this is that the flow stays attached far downstream on this geometry.

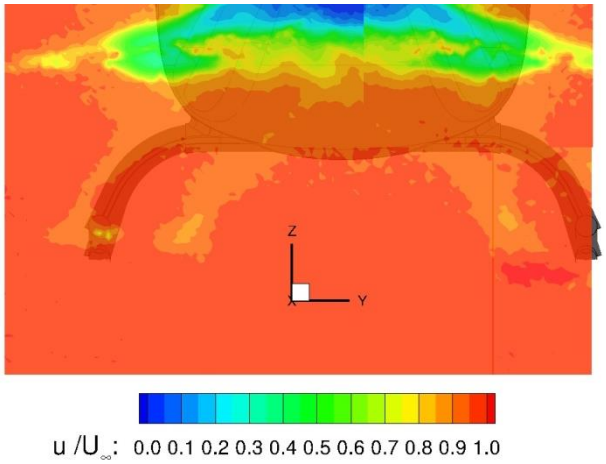


**Figure 11: Normalized time-averaged axial velocity component in the aft wake of the skid landing gear and the back door section; measured with PIV at P1.**

For this plane the averaged normalized z-component velocity is presented as well in Figure 12. It exhibits that in the region between the strakes a high positive velocity is induced. That is caused due to the far downstream attached flow. This results in a higher downforce which counteracts to the lift.

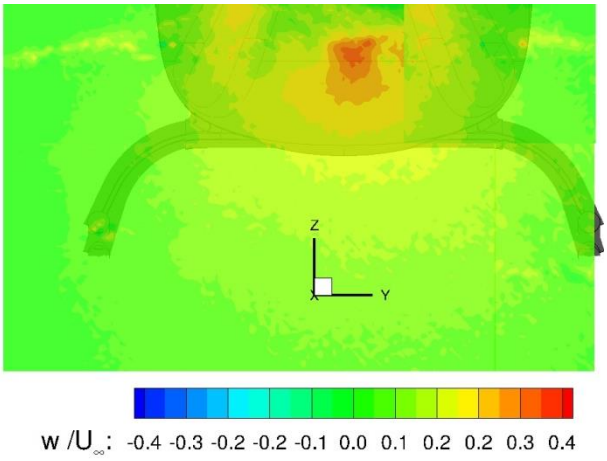


**Figure 12: Normalized time-averaged vertical velocity component in the aft wake of the skid landing gear and the back door section; measured with PIV at P1.**

Considering the plane downstream which is shown in Figure 13, the outer as well as the inner wake structures are still visible. The velocity deficit of the inner wake structures seems to be higher than those of the outer structure.

Regarding the wake flow of the aft body it can be stated that the influence of the strakes is clearly visible. Downstream of the strakes two symmetrical regions of reduced normalized axial velocity are detected with a higher velocity between them. This indicates that the flow stays attached further downstream among the strakes before it separates.

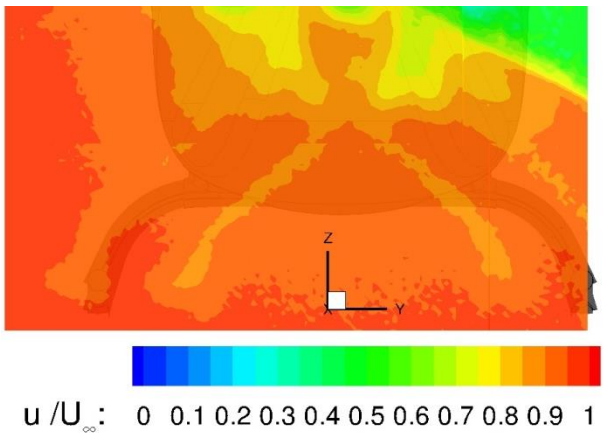


**Figure 13: Normalized time-averaged axial velocity component in the aft wake of the skid landing gear and the back door section; measured with PIV at P2.**

Figure 14 shows the time-averaged velocity distribution in the farthest downstream presented plane. In this plane the inner as well as the outer structure are still captured. The position of the lower boundary has changed slightly to greater values of the z-coordinate. Regarding the position of the back door section wake flow the difference compared to the upstream positioned plane is more distinctive. The region of reduced velocity downstream of the strakes is enlarged in the z-coordinate direction. Furthermore, the axial velocity increased in the region among the strakes. A greater axial velocity deficit occurs in direction of the positive z-coordinate. This indicates a small region of separated flow.

Figure 15 presents the averaged normalized axial velocity in the wake flow field downstream of the rotor head. It shows that the flow around the rotor head is asymmetrically. On the retreating side of the rotor head ($y < 0$), the region with reduced velocity is bigger. Additionally, it has to be noted that for the wind tunnel test a cyclic and collective pitch motion is set.

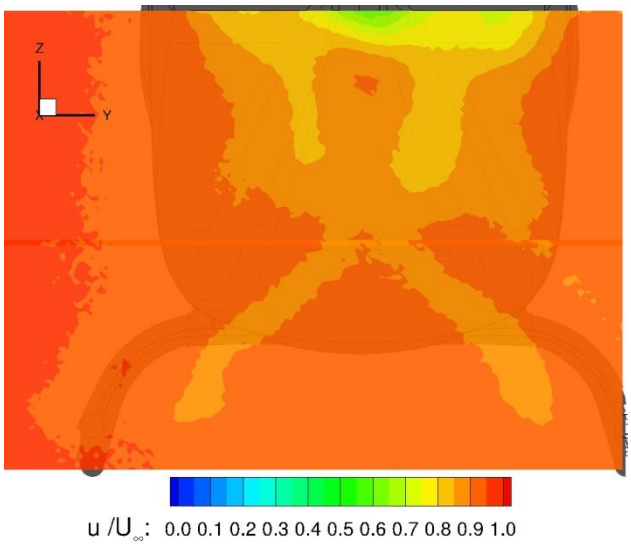


**Figure 14: Normalized time-averaged axial velocity component in the aft wake of the skid landing gear and the back door section; measured with PIV at P3.**

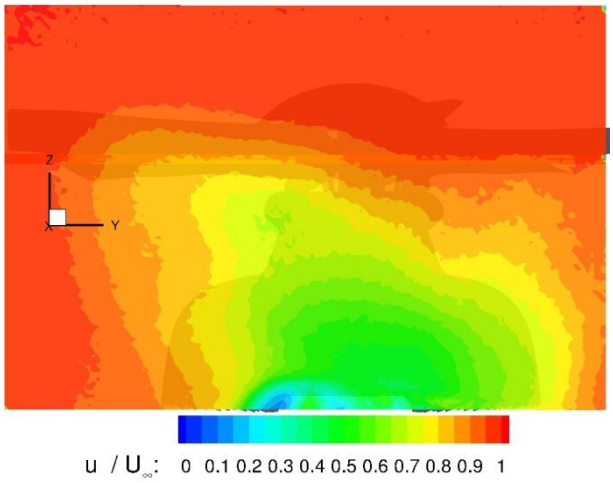


**Figure 15: Normalized time-averaged axial component in the aft wake of the skid landing gear and the back door section; measured with PIV at P4.**

### 4.2. Results of the URANS Simulations

In the following, numerical results are provided in order to complete the results for this configuration.

Figure 16 shows the normalized time-averaged axial velocity at the crossflow plane P2. For this simulation the SST turbulence model is used. The figure exhibits the influence of the skid landing gear well. Nevertheless, just the outer structure is visible. The inner structure is not resolved. But the shape of the outer structure differs with respect to the experiment. Furthermore, the model leads to a flow separation at the back cabin door section that occurs upstream compared to the experimental data.

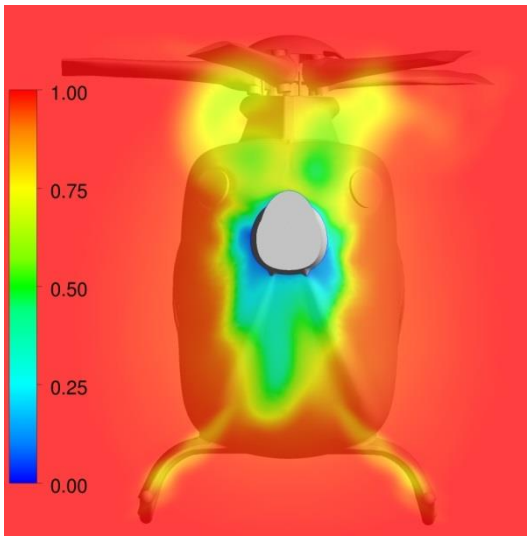


**Figure 16: Normalized time-averaged axial velocity component in the aft wake of the helicopter. URANS simulations with the SST turbulence model. It is shown at P2.**

Figure 17 depicts the normalized time-averaged axial velocity distribution at P2 as well. This simulation is performed with the SAS model. In this case the influence of the skid landing gear on the wake flow is still visible. Nevertheless, the inner wake structure is not captured by applying this model as well. Concerning the wake flow at the back cabin door section the SAS model predicts a smaller region with velocity deficit. Another interesting fact is, that the SAS model gives in the mean a symmetrical flow field while the SST simulation does not.

It has to be kept in mind that the presented calculations have been performed as fully turbulent simulations. As previous experimental investigations have shown laminar-turbulent transition takes place at the helicopters cabin. This will influence the boundary layer state at the back cabin door section and for this reason the separation.

Comparing the wake flow of the rotor head in the mean velocity distribution a similar flow field can be determined. Both results show an asymmetric wake flow field as the experimental data do.

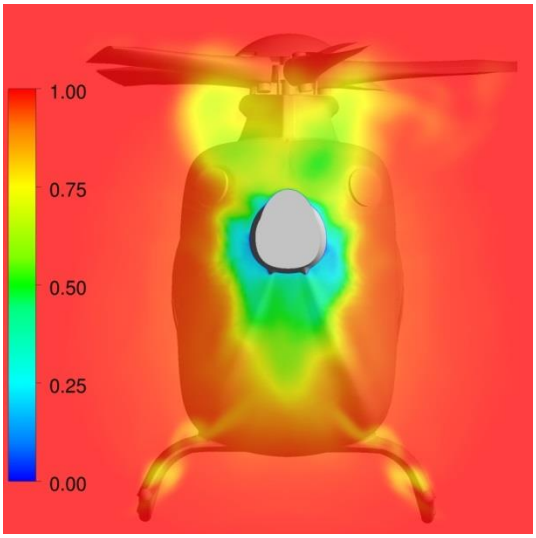


**Figure 17: Normalized time-averaged axial velocity component in the aft wake of the helicopter. URANS simulations with the SAS model. It is shown at P2.**

Concerning the capturing of the vortical coherent structures in the wake flow, iso-surfaces for a Q-criterion [10] level of $100000\,s^{-}2$ are shown in Figure 18. They are colored by the eddy viscosity ratio. High values represent a high level of modelled turbulence and vice versa. The result in Figure 18 is obtained by an SST turbulence model simulation. It is shown that the small coherent structures in the wake flow of the helicopter are damped due to the high turbulence eddy viscosity. That is why for a detailed investigation of the wake flow regarding unsteady phenomena this modelling approach may be unrewarding.

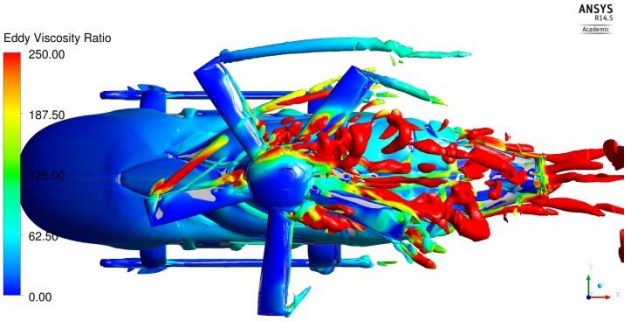


**Figure 18: Plan view of the vortical structures around the helicopter configuration for the result with the SST turbulence model; Q-criterion at $100000\,s^{-2}$ colored by the eddy viscosity ratio.**

For this purpose, a simulation with the SAS turbulence model is performed. Figure 19 shows that the eddy viscosity ratio is less compared to them of the SST turbulence model simulation. For this reason, smaller coherent structures occur in the wake flow field of the helicopter. Especially, observing the flow field downstream it can be seen that less coherent vortical structures are dissipated, compared to the results with the overpredicted turbulence of the SST turbulence model.

Nevertheless, the capturing of the blade tip vortices is similar for both turbulence models.

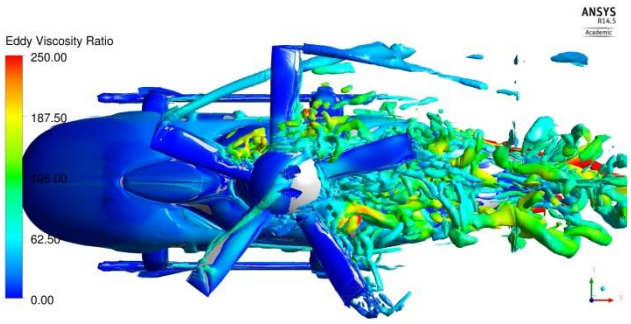


**Figure 19: Plan view of the vortical structures around the helicopter configuration for the result with the SAS model; Q-criterion at $100000\,s^{-2}$ colored by the eddy viscosity ratio.**

## 5. CONCLUSION

For flight comfort and safety issues the accurate determination of the helicopter wake flow field is significant. Especially, capturing unsteady phenomena is hard to achieve by applying computational fluid dynamics due to the variety of physical effects occurring in the flow field. Furthermore, the dissipative discretization error as well as turbulence models can diminish the strength of the coherent structures during the downstream convection too much. In order to determine the wake flow field experimental and numerical investigations have been performed. The experimental data were used to characterize and analyze the flow field in the aft wake region. The numerical simulations are conducted with the SST and the SAS model. The experimental data were compared to the numerical results.

The PIV results of the skid landing gear wake flow show an inner and an outer wake structure. The outer structure corresponds to the downstream positioned crossbeam. This structure could also be provided by the numerical simulations. The inner structure is not resolved by the chosen numerical approach. Concerning the wake flow of the back door section a larger region of separated flow can be detected from the numerical results compared to the experimental data. The separated flow region is smaller for the calculation with the SAS model than for the SST turbulence model. Furthermore, the normalized time-averaged velocity distribution in the wake flow of the back door section obtained by the SST turbulence model is asymmetric compared to the results of the SAS model which is symmetric. The mean wake flow of the rotor head shows similar asymmetric behavior for both, the numerical results and the experimental data. Nevertheless, using the Q-criterion to visualize the coherent vortical structures in the wake flow of the rotor head the scale resolving capability of the SAS model compared to the SST turbulence model becomes visible. Downstream of the rotor head, the SAS model captures smaller coherent structures.

In order to improve the accuracy of the numerical results in the wake region for the skid landing gear as well as the back door section a transition modeling will be applied. This will lead to changes in the shape of the boundary layer profiles. Furthermore, as stated above the separation is influenced by the shape of the boundary layer also. Including transition modelling shall counteract this lack in the modelling. Additionally, a zonal large eddy simulation can be performed to capture smaller coherent structures during the downstream flow convection [11].

## 6. REFERENCES

[1] R. Steijl and G. N. Barakos, "Computational Study of Helicopter Rotor-Fuselage Aerodyanmic Interaction," *AIAA Journal*, vol. 47, no. 9, 2009.

[2] M. Grawunder et al, "Optimized skid-landing-gears for twin-engine-light-utility helicopter," in *European Rotorcraft Forum*, 2013.

[3] M. Grawunder et al, "Helicopter Aft-Body Drag Reduction by Passive Flow Control," in *European Rotorcraft Forum*, 2014.

[4] M. Grawunder et al, "Flow Simulation of a Five Bladed Rotor Head," in *New Results in Numerical and Experimental Fluid Mechanics IX*, Springer, 2014, pp. 235-243.

[5] P. W. Li Xu, "High Order Accurate Low Dissipation Method for Unsteady Compressible Viscous Flow Computation on Helicopter Rotor in Forward Flight," *Journal of Computational Physics*, vol. 258, pp. 470-488, 2014.

[6] Q. e. a. Zhang, "Advanced CFD-based Optimization Methods Applied to the Industrial Design Process of Airframe Components at Airbus Helicopters,"

*American Helicopter Society 70th Annual Forum*, 2014.

[7] ANSYS, Inc., "ANSYS help system," 2014.

[8] F. R. Menter, "Two-equtation Eddy-Viscosity Turbulence Models for Engeneering Applications," *AIAA Journal*, vol. 32, no. 8, pp. 1598-1605, 1994.

[9] F. Menter and Y. Egorov, "The Scale-Adaptive Simultion Method for Unsteady Turbulent Flow Predictions. Part 1: Theory and Model Description," *Journal Flow Turbulence and Combustion*, vol. 85, pp. 113-138, 2010.

[10] J. Jeong and F. Hussain, "On the identification of a vortex," *Journal of Fluid Mechanics 285*, pp. 69-94, 1995.

[11] M. Stuhlpfarrer et al, "Numerical and Experimental Investigation of the Propeller Characteristics of an Elecrtically Powered Ultra-Light Aircraft," in *DLRK*, Augsburg, 2014.